Chapter 6

Plasma Loop Merging and the Two-Wire Problem

Chapter 5 presents a general theorem of Hamiltonian mechanics concerning the role of action integrals in systems with periodic motion. Keeping this formalism in mind, we now attempt to explain the coalescence of the spider legs in the Caltech Spheromak Experiment into a single axisymmetric structure. Recall from Sec. 1.4.2 that Taylor's theory of magnetic relaxation predicts this evolution towards the axisymmetry of the magnetic field boundary conditions. This explanation is macroscopic and based on helicity-conservation arguments; our approach will be microscopic to identify the mechanism behind the transition. We will study the trajectories of particles at the edge of or just outside of a spider leg; the behavior of such particles will be taken as indicative of the evolution of the spider leg boundary. We find that, when multiple plasma loops are present, the trajectories can be divided into two classes: those that are essentially confined to the vicinity of one loop and those that are shared more symmetrically between loops. When time dependence is added to the system, trajectories can transition from one class to the other. Obviously, transitions from confined to symmetric orbits would indicate the onset of loop merging, but such transitions occur only when the induced electric field takes a particular form. The ultimate success of the model in explaining the merging thus depends critically on the actual induced electric field in the experiments, which, in all likelihood, must be determined experimentally. Note that this same analysis also applies to dual-loop merging experiments on the Caltech Solar Loop Experiment.

The electromagnetic fields of the Caltech experiments are quite complex, and we will employ several approximations to make the problem tractable. Both the Spheromak and Solar experiments produce plasma loops arching from anode to cathode. These loops carry time-dependent currents and helical magnetic field lines. On the Spheromak Experiment, the spider legs are more tightly spaced on the inner disk than the outer annulus, while on the Solar Loop Experiment the two loops attract each other. Even establishing the electric and magnetic fields in either experiment is quite a challenge; determining the particle orbits in such fields is even more difficult. We seek model

magnetic and electric fields that capture the essential physics while remaining tractable. To this end, we begin with a modest model: straight plasma loops with no bias (axial) magnetic field. This approximation essentially treats the plasma loops as straight current-carrying wires and ignores the curved geometry and helical nature of the magnetic field lines.

In Sec. 6.1, we begin by analyzing a single wire, for which the particle trajectories all have the same qualitative behavior. We compute the action integral for planar motion and develop approximations for non-planar motion. We broach the difficulties of determining the induced electric field when the wire current changes in time, and we show how the Hamiltonian formalism of Chapter 5 applies to particles trajectories in such time dependent fields. In Sec. 6.2, we add a second wire, parallel to the first, and find a richer set of trajectories that fall into several classes: some are confined to one wire, and some are shared between both wires. When time-dependence is added to the two-wire scenario in Sec. 6.3, the induced electric field can cause transitions of confined orbits to shared orbits, but only if the induced electric field is anti-parallel to the wire current. We discuss the plausibility of such a field and show exactly how it would induce transitions.

6.1 Single Wire and $\mathbf{B} \sim \hat{\phi}/r$ Fields

Before attempting to study particle orbits in a system of plasma loops, it is best to first understand orbits about a solitary wire. Such orbits are of the type described in Chapter 5: the particle executes periodic radial motion but increments in the axial and angular coordinates. Fig. 6.1.a depicts planar electron motion about a wire for which there is no angular motion while Fig. 6.1.b depicts electron motion with non-zero angular momentum. We shall first discuss various occurrences of the magnetic field $\mathbf{B} \sim \hat{\phi}/r$. The action integral for planar orbits will then be evaluated in closed form, leading to an exact expression for the drift velocity. Approximate results are derived for non-planar orbits. The case of a time-dependent current is then explored, and issues concerning the induced electric field are discussed.

The magnetic field of a straight, infinitely thin wire carrying a current I is given by Ampere's law:

$$\mathbf{B} = \frac{\mu_0 I}{2\pi r}\hat{\phi}. \tag{6.1}$$

However, this magnetic field is not limited to infinitely thin wires. In general, the magnetic field for any axisymmetric, poloidal current density is $\mathbf{B}(r) = \mu_0 I(r)/(2\pi r)\hat{\phi}$, where $I(r) = \int_0^r 2\pi r' J_z(r')dr'$, which scales as $1/r$ wherever $J_z(r) = 0$. This includes the vacuum region outside any axisymmetric current channel as well as the interior of a toroidal solenoid. More generally, $\mathbf{B}$ decays like a $1/r$ field when $J_z(r) \ll I(r)/(2\pi r^2)$, for then

$$\frac{dB_\phi}{dr} = -\frac{\mu_0 I(r)}{2\pi r^2} + \mu_0 J_z(r) \approx -\frac{\mu_0 I(r)}{2\pi r^2}. \tag{6.2}$$

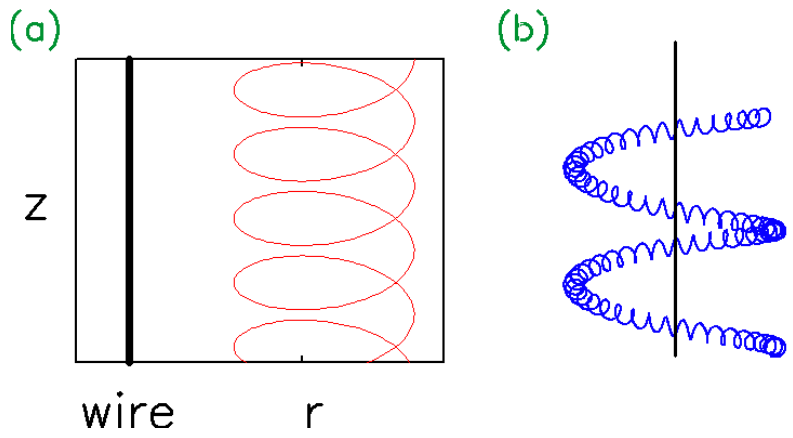

Figure 6.1: (a) An electron executes planar motion in the magnetic field of a current-carrying wire (b) A three-dimensional plot of an electron orbit with non-zero angular momentum.

The term $\mu_0 I(r)/2\pi r$ of Eq. (6.2) is $\mu_0/2$ times the average current density up to a radius r, so the condition $J_z(r) \ll I(r)/(2\pi r^2)$ requires that the local current density be much smaller than the average current density up to that radius. This condition will most likely be satisfied at the edge of current channels such as those described in Ref. [105]. Thus, $\mathbf{B} \sim \hat{\phi}/r$ both in the vacuum region outside of a current channel and also at the channel's edge. We also expect the field outside a filamentary but curved current channel to scale as $\mathbf{B} \sim \hat{\phi}/r$ wherever the distance to the channel is much smaller than the channel's radius of curvature. Clearly, many physical scenarios can have magnetic fields that behave approximately like $1/r$ fields, and the results presented here may have broad applications.

6.1.1 The Action and Drift Velocity for Planar Orbits

We now calculate the action variable J, the drift velocity, and magnetic flux of planar trajectories around a wire. For any toroidal magnetic field, there exists a class of planar orbits that is confined to a plane containing the wire [106]. This follows from conservation of angular momentum $P_\phi = mr^2\dot{\phi}$ because planar orbits have $P_\phi = 0$, which immediately implies $\dot{\phi} = 0$. For such trajectories, we relate results obtained in Chapter 5 for fields $\mathbf{B} = B_z(x)\hat{z}$ to orbits in toroidal fields $\mathbf{B} = B_\phi(r)\hat{\phi}$ by making the identifications $x \leftrightarrow r$, $y \leftrightarrow -z$, and $\hat{z} \leftrightarrow \hat{\phi}$.

We first establish the Hamiltonian and basic orbit properties. We use the vector potential

$$\mathbf{A} = A_z(r)\hat{z} = -\left(\int_R^r B(r')dr'\right)\hat{z} = -\frac{\mu_0 I}{2\pi}\ln\frac{r}{R}\hat{z}, \tag{6.3}$$

where R is an arbitrary radius that affects $\mathbf{A}$ only by the addition of a constant. To simplify constants, we introduce the characteristic velocity $\beta := \mu_0 Ie/2\pi m$ [106]. The canonical momenta

are

$$P_r = m\dot{r}, \tag{6.4}$$

$$P_\phi = mr^2\dot{\phi}, \tag{6.5}$$

$$P_z = m\dot{z} + (-e)A_z(r) = m\dot{z} + m\beta \ln \frac{r}{R}, \tag{6.6}$$

and the Hamiltonian is

$$H = \frac{P_r^2}{2m} + \frac{P_\phi^2}{2mr^2} + \frac{(P_z - m\beta \ln(r/R))^2}{2m}. \tag{6.7}$$

P_z, P_ϕ, and H are conserved along trajectories. For planar orbits, we set $P_\phi = 0$ and use the Hamiltonian

$$H = \frac{P_r^2}{2m} + \frac{(P_z - m\beta \ln(r/R))^2}{2m}. \tag{6.8}$$

Every orbit has two radial turning points where $v_r = 0$ and a single radius at which $v_z = 0$. Denoting the inner turning point by r_- and the outer one by r_+, we set $P_r = 0$ in Eq. (6.8) and solve for r to obtain

$$r_\pm = R \exp\left[\frac{P_z \pm \sqrt{2mH}}{m\beta}\right]. \tag{6.9}$$

These turning points allow us to determine whether the guiding center approximation holds true for a particular trajectory. The guiding center approximation requires that the fractional change in the magnetic field be small over the course of a gyration: $\delta B/B \ll 1$. The fractional change from the outer turning point to the inner one is

$$\frac{\delta B}{B} = \frac{B(r_-) - B(r_+)}{B(r_+)} = e^{2v/\beta} - 1, \tag{6.10}$$

which gives the simple condition $v \ll \beta$. Note that, due to the lack of an inherent length scale associated with the magnetic field, this condition is completely independent of the electron's position. We define the guiding center radius $r_{\rm gc}$ in analogy to Eq. (5.90) as the radius at which the axial velocity v_z vanishes:

$$r_{\rm gc} = R \exp\left(\frac{P_z}{m\beta}\right). \tag{6.11}$$

For orbits with $v \ll \beta$, this radius coincides with the gyrocenter radius [106]. This definition relates R and P_z, neither of which is a physical quantity, to a physical location along an orbit.

For planar orbits, the action integral,

$$J(H, P_z) = \oint \sqrt{2mH - \left(P_z - m\beta \ln \frac{r}{R}\right)^2}\, dr, \tag{6.12}$$

can be evaluated exactly using the substitution

$$\cos\theta = \frac{P_z - m\beta \ln r/R}{\sqrt{2mH}}. \tag{6.13}$$

θ is simply the angle the velocity vector makes with the z axis; note that $\theta = 0$ at r_-, $\theta = \pi/2$ at $r_{\rm gc}$, and $\theta = \pi$ at r_+. We can solve Eq. (6.13) for r as a function of θ:

$$r = r_{\rm gc} \exp\left[-\frac{v}{\beta}\cos\theta\right]. \tag{6.14}$$

The action variable can be evaluated by observing that $P_r = mv_r = mv\sin\theta$ and then integrating by parts:

$$J = \oint P_r dr = \oint mv\sin\theta \frac{dr}{d\theta} d\theta = -\oint mv\cos\theta r d\theta. \tag{6.15}$$

Then, using Eq. (6.14) and the integral representation of the modified Bessel function: $\int_0^\pi e^{x\cos\theta}\cos(n\theta)d\theta = \pi I_n(x)$ [107, Eq 9.6.19], we find that

$$J = 2\pi r_{\rm gc} mv I_1\left(\frac{v}{\beta}\right). \tag{6.16}$$

Δt and Δz can both be computed by partial differentiation as per Eq. (5.4):

$$\Delta z = -\frac{\partial J}{\partial P_z} = -2\pi\frac{v}{\beta} r_{\rm gc} I_1\left(\frac{v}{\beta}\right), \tag{6.17}$$

$$\Delta t = \frac{\partial J}{\partial H} = 2\pi\frac{r_{\rm gc}}{\beta} I_0\left(\frac{v}{\beta}\right). \tag{6.18}$$

Note that Eqs. (6.17), (6.18), and (6.16) have a simple dependence on $r_{\rm gc}$ that could have been predicted beforehand using only dimensional analysis. This is so because the vacuum magnetic field lacks an inherent length scale. The substitution of Eq. (6.13) was apparently known to Wouters, who derived similar formulae for the betatron half-wavelength in his charge/mass separator [108].

The exact drift velocity, computed without appealing to the guiding center approximation, is

$$\mathbf{v}_d = \frac{\Delta z}{\Delta t}\hat{z} = -v\frac{I_1(v/\beta)}{I_0(v/\beta)}\hat{z}. \tag{6.19}$$

This formula is exact and holds for orbits where the guiding center approximation breaks down. The $v \ll \beta$ limit of Eq. (6.19) is $\mathbf{v}_d = -v^2/(2\beta)$, obtained by the small argument limit of the modified Bessel functions: $I_n(x) \approx (x/2)^n$ [107, Eq. 9.1.7]. Of course, this agrees with the grad-B drift of the guiding center approximation as discussed in Sec. 5.2.2. The $v \gg \beta$ limit of Eq. (6.19) is $\mathbf{v}_d \approx -v\hat{z}$, obtained by the large argument limit of the modified Bessel functions: $I_\alpha(x) \approx e^x/\sqrt{2\pi x}$ when $x \gg \left|\alpha^2 - 1/4\right|$ [107, Eq. 9.7.1]. Such electrons drift downward with a drift speed approaching

their full trajectory speed. We draw two conclusions from this. First, all electrons drift downward regardless of their velocity or the wire current, and, similarly, all ions drift upwards. The current driven by the drift flows in the same direction as the original wire current, so the wire current "bootstraps" itself. Secondly, larger currents have larger values of β and hence smaller drift velocities, so the bootstrap effect is actually greatest for small wire currents. Similar observations were made by Alfven on the limit of current channels [109].

6.1.2 Non-Planar Orbits

For non-planar orbits, the action integral,

$$J(H, P_z, P_\phi) = \oint \sqrt{2mH - P_\phi^2/r^2 - (P_z - m\beta \ln(r/R))^2}\, dr, \tag{6.20}$$

cannot be evaluated exactly as in the planar case, but we can perform a Taylor expansion about $P_\phi = 0$. This treats the kinetic energy of the angular motion as a perturbation of the planar problem. The first-order expansion is

$$J(J, P_z, P_\phi) \approx J_0(H, P_z) + \frac{1}{2} \oint \frac{(-P_\phi^2/r^2)dr}{\sqrt{2mH - (P_z - m\beta \ln(r/R))^2}}, \tag{6.21}$$

where $J_0(H, P_z)$ is the planar action integral given by Eq. (6.16). Using the substitution $u/R = R/r$, we get

$$J(J, P_z, P_\phi) \approx J_0(H, P_z) + \frac{1}{2} \oint \frac{(P_\phi^2/R^2)du}{\sqrt{2mH - (P_z + m\beta \ln(u/R))^2}}, \tag{6.22}$$

which can then be evaluated with the substitution $\sqrt{2mH}\cos\theta = P_z + m\beta \ln(u/R)$,

$$J(H, P_z, P_\phi) \approx J_0(H, P_z) - \frac{\pi P_\phi^2}{m\beta r_{\rm gc}} I_0\left(\frac{\sqrt{2mH}}{m\beta}\right) \tag{6.23}$$

$$= J_0(H, P_z) - \frac{P_\phi^2}{2mr_{\rm gc}^2}\Delta t_0. \tag{6.24}$$

Δt_0 is the period for planar motion given by Eq. (6.18). Note that the correction term in Eq. (6.24) contains the kinetic energy of angular motion, $P_\phi^2/(2mr^2)$, evaluated at $r = r_{\rm gc}$. Indeed, Eq. (6.24) could have been derived from Eq. (6.21) by approximating P_ϕ^2/r^2 as $P_\phi^2/r_{\rm gc}^2$ and then evaluating the resulting integral:

$$\frac{1}{2} \oint \frac{(-P_\phi^2/r_{\rm gc}^2)dr}{\sqrt{2mH - (P_z - m\beta \ln(r/R))^2}} = -\frac{P_\phi^2}{2mr_{\rm gc}^2} \oint \frac{dr}{\dot{r}_0} = -\frac{P_\phi^2}{2mr_{\rm gc}^2}\Delta t_0, \tag{6.25}$$

where $\dot{r}_0$ is the unperturbed radial velocity. We can think of Eq. (6.21) as an averaging of the perturbation over an unperturbed orbit, in which case Eq. (D.22) could be used to obtain an even

more accurate estimate of J.

The P_ϕ term in Eq. (6.24) provides the first-order correction to all quantities derived from J due to angular motion. For instance, in the $v \ll \beta$ limit, the drift velocity agrees with the guiding center approximation once the curvature drift is added to the dominant grad-B drift.

6.1.3 Time-Varying Currents

In preparation for the time-dependent two-wire problem, we consider particle motion in a time-varying $1/r$ magnetic field. The primary difficulty in this case is actually not the particle orbits themselves but rather determining the appropriate electric field to use. It is well-known that a time-varying magnetic field induces an electric field, but Faraday's law, $\nabla \times \mathbf{E} = -\partial_t \mathbf{B}$, only specifies the curl of $\mathbf{E}$, leaving $\mathbf{E}$ undetermined up to the addition of the gradient of a scalar. In the single-wire case, we can write $\mathbf{E}$ in terms of the potentials

$$\mathbf{E} = -\frac{\partial \mathbf{A}}{\partial t} - \nabla V = \frac{\mu_0 \dot{I}}{2\pi} \ln \frac{r}{R} \hat{z} - \nabla V, \tag{6.26}$$

using the vector potential of Eq. (6.3). We cannot proceed, however, because we have no prescription for determining V: there are no boundary conditions for $\mathbf{E}$ due to the infinite extend of the wire, its infinite thinness, and its lack of return current. In order to determine the electric field, these details, which could be ignored in the static case, must be specified [110, 111]; a solitary infinite wire carrying a time-dependent current is an ill-posed problem. In this section, we present two return currents for the wire and their possible relevance to the Caltech experiments.

Consider the configuration shown in Fig. 6.2.a, where the wire current is fed by two large planar disks; this configuration is similar to a toroidal solenoid. We also assume that the wire has a non-zero radius $r = a$. If all surfaces are perfectly conducting, then the tangential component of the electric field must vanish on the surface. The appropriate electric field is obtained from Eq. (6.26) by setting $V = 0$ and $R = a$:

$$\mathbf{E} = \frac{\mu_0 \dot{I}}{2\pi} \ln \frac{r}{a} \hat{z}. \tag{6.27}$$

$\mathbf{E}$ then satisfies the boundary conditions at the plates because it is axial, and it satisfies the boundary condition on the wire surface because it vanishes at $r = a$. This electric field is aligned with the wire current, and the associated Poynting flux in radially inward, suggesting that the source of energy for the circuit is located at $r = \infty$.

Now consider the configuration shown in Fig. 6.2.b where the current returns coaxially at radius $r = b$. For perfectly conducting surfaces, the axial electric field must vanish at both $r = a$ and $r = b$.

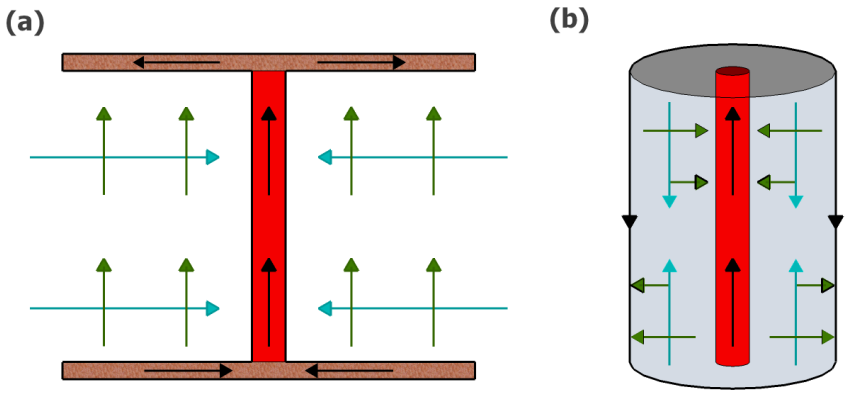

Figure 6.2: Two different possible returns for a wire: (a) two planar plates radially feed the wire and (b) a coaxial return. The direction of current flow is drawn in black, the electric field is drawn in green, and the Poynting vector is drawn in blue.

Evaluating Eq. (6.26) on these surfaces implies

$$E_z(r=a)=0 \quad \rightarrow \quad \left.\frac{\partial V}{\partial z}\right|_{r=a} = \frac{\mu_0 \dot{I}}{2\pi}\ln\frac{a}{R}, \tag{6.28}$$

$$E_z(r=a)=0 \quad \rightarrow \quad \left.\frac{\partial V}{\partial z}\right|_{r=b} = \frac{\mu_0 \dot{I}}{2\pi}\ln\frac{b}{R}, \tag{6.29}$$

V must also satisfy Laplace's equation because $\mathbf{E}$ satisfies Poisson's equation: $\nabla\cdot\mathbf{E}=0$. For azimuthal symmetry, $\nabla^2 V = 0$ has solutions of the form $V \sim z\ln r$. Matching the boundary condition, we have

$$V = \frac{\mu_0 \dot{I}(t)}{2\pi} z \ln\frac{r}{R}. \tag{6.30}$$

The axial component of the electric field vanishes, leaving a radial radial electric field,

$$\mathbf{E} = -\frac{\mu_0 \dot{I}(t)}{2\pi}\frac{z}{r}\hat{r}, \tag{6.31}$$

which is independent of R and the radii of the cable. Note that V breaks the axial symmetry of the configuration, and in particular there is a z position at which $\mathbf{E}$ vanishes. This location might be physically set by placing an electrical short between the inner and outer conductors. A zero in the radial (normal) electric field is also seen in the electrostatic field of a circuit, and the location of the zero depends on the circuit geometry [112]. Also note that the Poynting vector directs energy axially towards the zero of the electric field.

Neither the fields in Eq. (6.27) nor Eq. (6.31) are entirely accurate. Both fields are unbounded and rise to arbitrarily high values. Also, neither field truly satisfies Ampere's law because the displacement current $\epsilon_0\partial_t\mathbf{E}$ does not vanish. However, if we work in the limit of adiabatic slowness, then the displacement current, which is proportional to $\ddot{I}$ in both cases, can be ignored. For com-

pleteness, we note that the fields that fully satisfy Ampere's and Faraday's law are TEM modes; the electric field in Eqs. (6.27) and (6.31) are approximately equal to the sum of an ingoing wave and a reflected wave, the waves traveling radially and axially, respectively, and being reflected at $r = a$ and $z = 0$, respectively.

Which of these two field configurations most closely resembles the actual fields in the Caltech experiments is an open question. On the one hand, the plates that radially feed the wire in Fig. 6.2.a resemble the plasma electrodes on which each flux tube starts and ends. The boundary conditions imposed by these plates cannot be satisfied by the radial electric field in Eq. (6.31), and, from this argument, the field is likely to resemble the axial field of Eq. (6.27) bent into a curved geometry as depicted in Fig. 6.3. On the other hand, plasmas are liable to form thin sheaths at all the boundaries, and the electric field in the sheath is likely to be normal to the surface. In this case, the plasma might have a field structure shown in Fig. 6.4. Given the possible existence of sheaths, it is unlikely that the correct electric field can be easily derived from first principles, and in all likelihood an experimental measurement will be needed to determine the actual field.

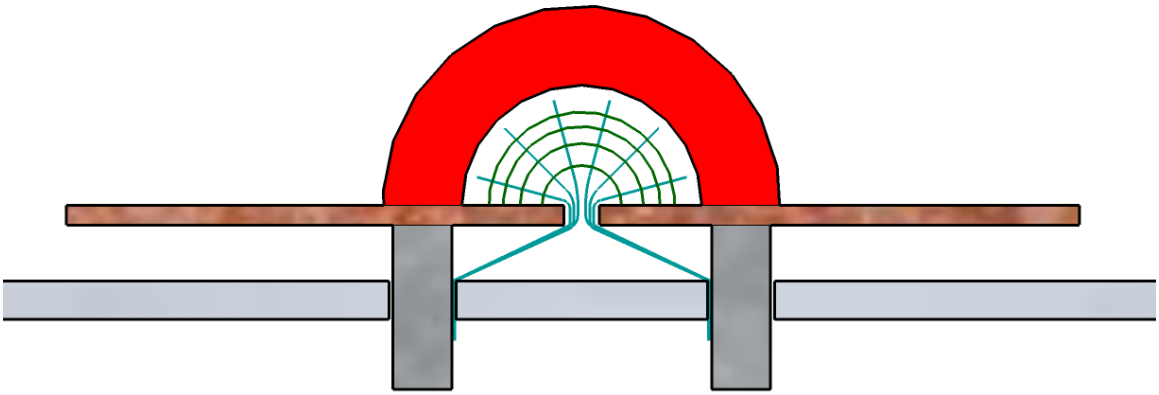

Figure 6.3: The Solar Loop Experiment might have an induced electric field that is "axial," as shown here by the green lines. The electric field begins and ends on the electrodes. The associated Poynting flux, shown by the blue lines, transports energy radially through the gap in the electrodes.

The induced electric field thus depends on the particulars of the setup, but we can still establish a reduced Hamiltonian for particle orbits and derive general properties without going into the full details. We leaving V arbitrary except for two requirements: that V is proportional to $\dot{I}$ and hence vanishes when the current is static, and that the current changes very slowly so that terms involving $\ddot{I}$ and $\dot{I}^2$ can be ignored. The exact Hamiltonian for particle motion is

$$H = \frac{P_r^2}{2m} + \frac{(P_z - m\beta(t)\ln(r/R))^2}{2m} - eV(r,z,t), \tag{6.32}$$

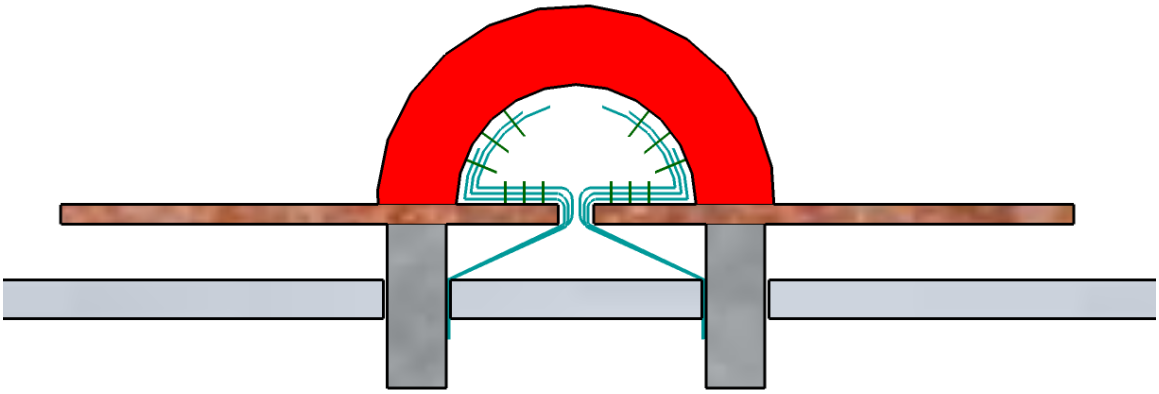

Figure 6.4: Alternatively, the Solar Loop Experiment might have an induced electric field that is "radial," as shown here by the green lines. The electric field lines are normal to the plasma surface. The associated Poynting flux transports energy axially along the flux tube.

The Hamiltonian now contains explicit time and z dependence, so H and P_z are no longer conserved quantities but instead evolve as

$$\dot{H} = \frac{\partial H}{\partial t} = \frac{P_z - m\beta \ln(r/R)}{m}\left(-m\dot{\beta}\ln\frac{r}{R}\right) - e\frac{\partial V}{\partial t} \tag{6.33}$$

$$\approx -m\dot{\beta}\dot{z}\ln\frac{r}{R} \tag{6.34}$$

$$\dot{P}_z = -\frac{\partial H}{\partial z} = -e\frac{\partial V}{\partial z}. \tag{6.35}$$

The term $\partial_t V$ in Eq. (6.33) is dropped because it is proportional to $\ddot{I}$. These equations give the instantaneous evolution of H and P_z and fluctuate over the course of a gyro-orbit. In Chapter 5, we developed a formalism to obtain the orbit-averaged equations of motion. Using Eq. (5.137) with J_0 being the action given by Eq. (6.16) for the static magnetic field:

$$J(H,P_z) \approx J_0\left(H - qV(r_{\rm gc},z,t) + \frac{m}{2}\left(\frac{\partial_r V}{B_z}\right)^2, P_z + m\frac{\partial_r V}{B_z}; \beta(t)\right) \tag{6.36}$$

$$\approx J_0\left(H + eV(r_{\rm gc},z,t), P_z + e\frac{r}{\beta}\partial_r V; \beta(t)\right). \tag{6.37}$$

The term $(m/2)\left(\partial_r V/B_z\right)^2$ is dropped because it was proportional to $\dot{I}^2$. Also, we have explicitly written the β dependence of J_0 because it will be needed below. We use Eq. (6.37) to compute the average evolution $\Delta H/\Delta t$ and $\Delta P_z/\Delta t$. We can compute ΔP_z and hence $\Delta P_z/\Delta t$ from Eq. (5.4):

$$\Delta P_z = \frac{\partial J}{\partial z} = \frac{\partial J_0}{\partial H}\left(e\frac{\partial V}{\partial z}\right) + \frac{\partial J_0}{\partial P_z}\left(e\frac{r}{\beta}\frac{\partial^2 V}{\partial r\partial z}\right) = \Delta t\left(e\frac{\partial V}{\partial z}\right) - \Delta z_0\left(e\frac{r}{\beta}\frac{\partial^2 V}{\partial r\partial z}\right), \tag{6.38}$$

$$\frac{\Delta P_z}{\Delta t} = \left(1 + \frac{r}{\beta}\frac{\Delta z_0}{\Delta t}\frac{\partial}{\partial r}\right)\left(e\frac{\partial}{\partial z}\right)V. \tag{6.39}$$

This is the average evolution of P_z, which is related to the instantaneous evolution in Eq. (6.35) by the averaging formula Eq. (D.22).

We can also work out the change in energy ΔH over one period of motion. We briefly return to the general Hamiltonian theory of Chapter 5 and assume that the Hamiltonian contains explicit time dependence, $H = H(\xi, P_\xi, \eta, P_\eta; t)$, but that adiabatic invariance of J is maintained. Then the action integral J contains explicit time-dependence, and

$$\frac{\partial J}{\partial t} = \oint \frac{\partial P_\xi}{\partial t} d\xi = \oint -\frac{\partial H/\partial t}{\partial H/\partial P_\xi} d\xi = -\oint \frac{\dot{H}}{\dot{\xi}} d\xi \tag{6.40}$$

$$= -\oint \dot{H} dt = -\Delta H. \tag{6.41}$$

We have made use of the fact that the total time derivative of H along a trajectory is equal to its partial time derivative. Applying this theorem to Eq. (6.37),

$$\Delta H = -\frac{\partial J}{\partial t} = -\frac{\partial J_0}{\partial H}\left(e\frac{\partial V}{\partial t}\right) - \frac{\partial J_0}{\partial P_z}\left(e\frac{r}{\beta}\frac{\partial^2 V}{\partial r \partial t}\right) - \frac{\partial J_0}{\partial t} \approx -\frac{\partial J_0}{\partial t} = -\dot{\beta}\frac{\partial J_0}{\partial \beta}, \tag{6.42}$$

since all other terms are proportional to $\ddot{\beta}$. The relationship between ΔH and $\dot{H}$ may not be apparent, but integrating Eq. (6.34) with respect to time over one period of unperturbed motion gives

$$\Delta H = \oint -m\dot{\beta}\dot{z}\ln\frac{r}{R} dt = -m\dot{\beta}\oint \ln\frac{r}{R} dz = -\frac{2\pi m\dot{\beta}}{\mu_0 I}\oint \mathbf{A}\cdot d\mathbf{r}. \tag{6.43}$$

As discussed in Sec. 5.1.8, we can pull $\dot{\beta}$ and $I(t)$ out of the integral sign because we can effectively hold these quantities constant over the course of a single period. Applying Eq. (5.160) with $V = 0$[1] to Eq. (6.43) and obtain

$$\Delta H = -q\frac{\dot{\beta}}{\beta}\frac{\partial J_0}{\partial q} = -\dot{\beta}\frac{\partial J_0}{\partial \beta}, \tag{6.44}$$

where the last step follows because q only appears the expression for J_0 in Eq. (6.16) through β.

We could further pursue the nature of particle orbits in these time-dependent fields, but this is not a fruitful task. The lessons that should be taken from this section are that time-dependent currents induce electric fields that can be difficult to compute and that require the global circuit geometry to be specified. Furthermore, the electric field might break some of the symmetries present in the static problem, causing previously conserved momenta to gradually evolve in time.

[1] We set $V = 0$ here because we are integrating Eq. (6.34) over an unperturbed trajectory.

6.2 The Two-Wire Problem

The previous section described particle orbits around a single solitary wire. We now turn our attention to trajectories in the magnetic field generated by two parallel wires carrying equal currents. Planar orbits still exist in the plane containing both wires, but now these planar orbits fall into several distinct classes. Some of these orbits are localized to one wire and resemble the orbits observed in the previous section for a single wire. Other orbits, however, are shared symmetrically between the two wires. This distinction between confined and symmetric orbits is exactly what is needed to describe the merging of two parallel plasma loops.

We will work in Cartesian coordinates with the z axis aligned with the wires and x being the direction separating the wires. Let the wires be located at $x = \pm a/2$ so that the wire separation distance is a. The magnetic field in the plane containing the wires is

$$\mathbf{B} = \frac{\mu_0 I}{2\pi}\left[\frac{1}{a/2+x} - \frac{1}{a/2-x}\right]\hat{y} = \frac{\mu_0 I}{2\pi}\frac{-2x}{a^2/4-x^2}\hat{y}. \tag{6.45}$$

We note that there is a magnetic null at $x = 0$ where the field vanishes; this null will play an important role is the classification of orbits. The vector potential can be chosen such that

$$\mathbf{A} = -\frac{\mu_0 I}{2\pi}\left[\ln\frac{a/2+x}{R} + \ln\frac{a/2-x}{R}\right]\hat{z} = -\frac{\mu_0 I}{2\pi}\ln\frac{a^2/4-x^2}{R^2}\hat{z}, \tag{6.46}$$

where R is again arbitrary. The canonical z momentum for an electron of charge $q = -e$ is

$$P_z = mv_z + m\beta\ln\frac{a^2/4-x^2}{R^2}, \tag{6.47}$$

and is conserved, yielding v_z as a function of x:

$$v_z(x) = \frac{1}{m}\left[P_z - m\beta\ln\frac{a^2/4-x^2}{R^2}\right]. \tag{6.48}$$

We will work with scaled variables, scaling distance by $a/2$, velocity by β, and momentum by $m\beta$. Since R is arbitrary, we set it equal to $a/2$ so that it is scaled to unity. Then, in scaled variables, Eq. (6.47) becomes

$$P_z = v_z + \ln\left(1-x^2\right). \tag{6.49}$$

From Eq. (6.49), we can derive the existence and location of turning points where the x motion reverses. These turning points exist because the magnitude of the z velocity v_z can never exceed the magnitude v of the total velocity, so the locations where Eq. (6.49) predicts $|v_z| = v$ denote turning points. We can find these turning points by setting v_z in Eq. (6.49) equal to either $\pm v$ and solving

for x:

$$x = \pm\sqrt{1 - e^{P_z \pm v}}. \tag{6.50}$$

The choice of $+$ and $-$ is independent between the two $\pm$ signs, so up to four turning points exist for any given orbit. These turning points come in mirrored pairs about the magnetic null $x = 0$. We shall show that one of these pairs exists for all orbits, while the second pair only exists if certain conditions are met.

When $P_z + v < 1$, all four turning points exists, and the orbit resembles those of a single wire. One set of turning points, which we denote by x_+, is given by choosing the $+$ sign in the exponential of Eq. (6.50):

$$x_+ = \pm\sqrt{1 - e^{P_z + v}}. \tag{6.51}$$

Since $P_z + v < 0$ by assumption, we have $\exp(P_z + v) < 1$, and the argument of the radical in Eq. (6.51) is positive. The second set of turning points, which we denote by x_-, is given by choosing the $-$ sign in the exponential in Eq. (6.50),

$$x_- = \pm\sqrt{1 - e^{P_z - v}}. \tag{6.52}$$

The argument of the radical in Eq. (6.52) is also positive, because $P_z - v < P_z + v$, so

$$1 - \exp(P_z - v) > 1 - \exp(P_z + v) > 0. \tag{6.53}$$

This argument also establishes that $|x_-| > |x_+|$, so the turning points $\pm x_+$ lie between the turning points $\pm x_-$. In such orbits, the particles rattle back and forth between an inner and outer turning point and never crosses the magnetic null at $x = 0$. Such a particle is thus "trapped" in one half of the plane and is "confined" to one of the two wires. These orbits resemble the orbits seen in Sec. 6.1, and an example of such an orbit is plotted in Figs. 6.5.a and 6.5.b.

When $P_z + v > 0$, the inner turning points $\pm x_+$ given by Eq. (6.51) fail to exist, and the particle is instead confined by the two outer turning points $\pm x_-$ given by Eq. (6.52). This constitutes a new class of trajectories not seen in the single wire case. The non-existence of the inner turning points x_+ follows simply by noting that the argument of the radical in Eq. (6.51) is negative because $P_z + v > 0$. The two outer turning points are still defined; to see this, we prove that $P_z - v < 0$ for any orbit using Eq. (6.49),

$$P_z - v > P_z - v_z(x) = \ln(1 - x^2) < 0. \tag{6.54}$$

In physical terms, the outer turning points always exist because the magnetic field becomes infinitely

strong at the wires[2], so all orbits are deflected from the wires. The inner turning points, however, are not always defined because some particles reach the magnetic null at $x = 0$. As the particle crosses the null, the sign of field reverses, reversing the radius of curvature of the trajectory as well. The particle then moves back and forth between the two outer turning points; such an orbit is symmetric between the two wires and is not confined to a single flux tube; compare Figs. 6.5.b and 6.5.c.

We can further classify symmetric orbits based on the direction of their drifts. Figures. 6.5.c through 6.5.f show several examples of symmetric orbits; some orbits, such as that shown in Fig. 6.5.c, have the same drift direction as in the single wire case, but other orbits, such as that shown in Figs. 6.5.e and 6.5.f, have the opposite drift. To derive this distinction, we first solve for the x positions where $v_z(x) = 0$:

$$x = \pm\sqrt{1 - e^{P_z}}. \tag{6.55}$$

These x positions are not defined when $P_z > 0$. For such cases, v_z is never zero but rather always positive. The particle never turns around in the z direction; it bounces back and forth between the two turning points while snaking its way up the z axis as shown in Fig. 6.5.f. This drift is in the opposite direction as the drift of a particle around a single wire. If, however, $P_z < 1$, then the particle has $v_z < 0$ for part of its orbit. Such particles can drift in either the positive or negative z direction, as demonstrated by Fig. 6.5.c and 6.5.e. There is a special class of orbits that have no net movement in the z direction but rather make figure-eight motion; an example is shown in Fig. 6.5.d.

The distinction between confined and symmetric orbits can be explained using effective potentials [2, sec. 119]. The Hamiltonian for a planar orbits between two wires is, for an electron of charge $q = -e$

$$H = \frac{P_x^2}{2m} + \frac{(P_z^2 + eA_z(x))^2}{2m}. \tag{6.56}$$

This is a two-dimensional Hamiltonian system, but, because z is ignorable, we can instead view it as a one-dimensional system in x with a parameter P_z. In this one-dimensional system, the particle is confined in an effective potential

$$U_{\text{eff}} = \frac{1}{2m}\left(P_z - m\beta \ln \frac{a^2/4 - x^2}{R^2}\right)^2, \tag{6.57}$$

where Eq. (6.46) has been used. We can express this effective potential in terms of scaled coordinates, with scaled energy as $\overline{U} = U/(m\beta^2)$,

$$\overline{U}_{\text{eff}} = \left(P_z - \ln(1 - x^2)\right)^2 \tag{6.58}$$

The shape of this potential is determined by the value of P_z. Fig. 6.6.a plots U_{eff} when $P_z > 0$; in this case the potential well is always concave up, and the magnetic null at $x = 0$ is a minimum of the

[2]If the wires were not infinitely thin, this would not be the case, and orbits could also pass into the wire.

potential. Fig. 6.6.b, however, plots U_{eff} when $P_z < 0$. The potential well develops a central bump, and the null is now a local maximum. It is also clear that particles of low energy will be confined to one of the smaller side wells, whereas particles of sufficient energy will travel over the null and will not be confined to either side well.

In summary, we have five types of motion:

- Snaking motion, shown in Fig. 6.5.f, where the orbit always moves in the positive z direction and bounces back and forth symmetrically between the two wires
- Jigsaw motion, shown in Fig. 6.5.e, in which the orbit still bounces symmetrically between the wires and has a positive drift but also travels in the negative z direction for certain periods of time
- Closed figure-eight orbits, shown in Fig. 6.5.d where the electron has no net z motion
- Loopy motion, shown in Fig. 6.5.c, in which the orbit is symmetrical but has a negative z drift
- Confined motion, shown in Fig. 6.5.a and 6.5.b, where the orbit never crosses the magnetic null at $x = 0$ and drifts downward as in the single-wire case

These results are also summarized in a parameter space plot in Fig. 6.7. To make the plot more intuitive, we express P_z in terms of x_- via Eq. (6.52). For instance, the condition $P_z + v < 0$ can be recast as $v < -(1/2)\ln(1 - x_-^2) < 0$, and the condition $P_z > 0$ can be recast as $v < -\ln(1 - x_-^2)$. Also plotted in Fig. 6.7 are several isolated points where the conditions for a closed orbit have been calculated numerically.

6.3 Time Dependence and Orbit Transitions

The previous section established distinct classes of orbits in the plane between two parallel current-carrying wires. However, in this static system, orbits cannot transition between the different classes. We therefore seek a mechanism that causes orbits confined to one-half of the plane to drift inward towards the magnetic null where they can transition to symmetric orbits. An axial electric field induced by two plasma loops attracting one another provides exactly such a mechanism.

6.3.1 Axial Electric Fields

Trajectories will be drawn to the magnetic null line if an axial electric field points in the negative z direction anti-parallel to the current because the $\mathbf{E} \times \mathbf{B}$ drift will be inward towards $x = 0$. This scenario is similar to Speiser's current sheet [113] where an electric field anti-parallel to the current causes particle to drift towards the null sheet where they are then accelerated by the electric field

along the null sheet. In order to achieve such a transition, we must have an electric field that is (i) axial and (ii) pointing in the negative z direction anti-parallel to the wire current.

In Sec. 6.1.3, we discussed possible electric fields associated with a single wire carrying a time-dependent current. In particular, we considered two configurations, shown in Fig. 6.2, for which the induced electric fields are entirely different, as shown by comparing Eqs. (6.27) and (6.31). An argument was made for the axial field, Eq. (6.27), based on the fact that the radial component must vanish at the electrodes, which cannot be satisfied by the radial electric field in Eq. (6.31). Also, as we shall see below, there must be an axial component to the electric field when the wires attract and move towards each other, so a purely radial electric field is not possible. However, the actual experiment has curved, finite geometry, as suggested by Figs. 6.3 and 6.4, and also probably involves sheaths, which makes determining the actual field configuration very difficult. We will proceed using an axial electric field but acknowledge that the actual field may be different.

Even if $\mathbf{E}$ is assumed to be axial, relative motion between the wires is necessary for $\mathbf{E}$ to be anti-parallel. To see this, assume that $\mathbf{E}$ is axial and that the current $I(t)$ is increasing but that the wires are stationary; we shall show that the induced electric field is *parallel* to the current and draws particles *away* from the magnetic null. For a current profile I(t), we have, from the vector potential Eq. (6.46),

$$\mathbf{E} = -\frac{\partial \mathbf{A}}{\partial t} = \frac{\mu_0 \dot{I}}{2\pi} \ln \frac{a^2/4 - x^2}{R^2} \hat{z}. \tag{6.59}$$

ρ must be selected so that $\mathbf{E}$ satisfies the boundary condition at the plasma surface. If the plasma has radius ρ, then the boundaries of the loops are $x = \pm(-a/2 + \rho)$; see Fig. 6.8. If $\mathbf{E}$ is to vanish at these locations, then we must set $R = a^2/4 - (a/2 - \rho)^2$. Then

$$\mathbf{E} = \frac{\mu_0 \dot{I}}{2\pi} \ln \frac{a^2/4 - x^2}{a^2/4 - (a/2 - \rho)^2} \hat{z}, \tag{6.60}$$

and $\mathbf{E}$ points in the positive z direction everywhere. An increasing plasma current cannot explain the merging of the two loops; if anything, the increase in current would cause the orbits to constrict radially.

One can have an anti-parallel electric field if the inner boundaries of the plasma loops move towards each other; that is, if ρ increases or a decreases in Fig. 6.8. This is certainly the case in the Solar Loop Experiment, where the plasma loops attract. This is also true on the Spheromak side for plasma moving towards the cathode because the loops are more tightly spaced there. We assume that the plasma loops are perfectly conducting so that the electric field *in the co-moving frame of the loop edge* must vanish. Since this surface is moving due to the loops' attraction, the electric field in the lab frame is not zero but is related to the field in the co-moving frame by $\mathbf{E}' = \mathbf{E} + \mathbf{v} \times \mathbf{B} = 0$, where $\mathbf{E}'$ denotes the electric field in the moving boundary's frame. Since $\mathbf{E}' = 0$ by assumption, the lab frame electric field at the boundary is $\mathbf{E} = -\mathbf{v} \times \mathbf{B}$. The boundary located at $x = -a/2 + \rho$

has a velocity of $\mathbf{v} = (-\dot{a}/2 + \dot{\rho})\hat{x}$; using this $\mathbf{v}$ and the magnetic field of Eq. (6.45) gives $\mathbf{E}$ at the boundary

$$\mathbf{E} = -\mathbf{v} \times \mathbf{B} = -\left[(-\dot{a}/2 + \dot{\rho})\hat{x}\right] \times \left[\frac{\mu_0 I}{2\pi} \frac{-2(-a/2+\rho)}{a^2/4 - (-a/2+\rho)^2}\hat{y}\right] \tag{6.61}$$

$$= -(-\dot{a}/2 + \dot{\rho})\frac{\mu_0 I}{2\pi}\frac{2(a/2-\rho)}{\rho(a-\rho)}\hat{z}. \tag{6.62}$$

This electric field is anti-parallel to the current and induces drifts towards the magnetic null.

6.3.2 Computing the Field

To continue, we assume that the electric field is entirely axial and has the boundary condition given by Eq. (6.62). We then use Faraday's law to compute $\mathbf{E}$ everywhere in the plane. Using the magnetic field in Eq. (6.45) and an axial electric field, we have

$$\nabla \times \mathbf{E} = -\frac{\partial E_z}{\partial x}\hat{y} = -\frac{\partial \mathbf{B}}{\partial t} = \left[\frac{\mu_0 \dot{I}}{2\pi}\ln\frac{2x}{a^2/4 - x^2} - \frac{\mu_0 I}{2\pi}\frac{2x}{(a^2/4-x^2)^2}\frac{a\dot{a}}{2}\right]\hat{y}. \tag{6.63}$$

Performing the x integral,

$$E_z = \frac{\mu_0 \dot{I}}{2\pi}\ln\left(a^2/4 - x^2\right) + \dot{a}\frac{\mu_0 I}{2\pi}\frac{a/2}{a^2/4 - x^2} + C, \tag{6.64}$$

where C is a constant of integration that must be determined by the boundary conditions. Indeed, the value of C will determine the ultimate polarity of E_z and hence the direction of the $\mathbf{E} \times \mathbf{B}$ drift! Evaluating Eq. (6.64) at $x = -a/2 + \rho$ and setting it equal to Eq. (6.62) determines C:

$$\frac{\mu_0 \dot{I}}{2\pi}\ln\left(\rho(a-\rho)\right) + \dot{a}\frac{\mu_0 I}{2\pi}\frac{a/2}{\rho(a-\rho)} + C = -(-\dot{a}/2 + \dot{\rho})\frac{\mu_0 I}{2\pi}\frac{2(a/2-\rho)}{\rho(a-\rho)}. \tag{6.65}$$

Solving for C and substituting into Eq. (6.64) gives

$$E_z = \frac{\mu_0 \dot{I}}{2\pi}\ln\frac{a^2/4 - x^2}{\rho(a-\rho)} + \dot{a}\frac{\mu_0 I}{2\pi}\left(\frac{a/2}{a^2/4 - x^2} - \frac{1}{a-\rho}\right) - \dot{\rho}\frac{\mu_0 I}{2\pi}\frac{2(a/2-\rho)}{\rho(a-\rho)}, \tag{6.66}$$

the induced electric field between two wires when the current, wire separation, and wire radius change in time.

The ultimate polarity of the electric field cannot be determined until the three quantities $\dot{I}$, $\dot{a}$, and $\dot{\rho}$ are specified. We can see that the $\dot{I}$ term of Eq. (6.66) is positive when $\dot{I}$ is positive, but the $\dot{a}$ and $\dot{\rho}$ terms can make the induced electric field negative. Unfortunately, a and r are not easily determined to great accuracy. For the purposes of this analytic study, however, we shall assume

that each of these three quantities changes self-similarly on the same time scale. That is,

$$\dot{I} = \frac{I}{\tau} \qquad \dot{a} = -\frac{a}{\tau} \qquad \dot{\rho} = \frac{\rho}{\tau}. \tag{6.67}$$

This allows us to rewrite Eq. (6.66) as

$$E_z = \frac{\mu_0 I}{2\pi\tau}\left[\ln\frac{a^2/4 - x^2}{\rho(a-\rho)} - \left(\frac{a^2/2}{a^2/4 - x^2} - \frac{a}{a-\rho}\right) - \frac{2(a/2-\rho)}{(a-\rho)}\right]. \tag{6.68}$$

We now introduce normalized lengths $\bar{x} = x/(a/2)$ and $\bar{\rho} = \rho/(a/2)$ and a normalized field strength $\overline{E} = 2\pi\tau E/\mu_0 I$ and rewrite Eq. (6.68) as

$$\overline{E}_z = \ln\frac{1-\bar{x}^2}{\bar{\rho}(2-\bar{\rho})} - \left(\frac{2}{1-\bar{x}^2} - \frac{2}{2-\bar{\rho}}\right) - \frac{2(1-\bar{\rho})}{(2-\bar{\rho})}. \tag{6.69}$$

The electric field profile then depends on the dimensionless quantity $\bar{\rho}$. We plot this profile for several values of $\bar{\rho}$ less than one in Fig. 6.9. For a wide range of $\bar{\rho}$, the electric field is everywhere negative in the plane between the two wires. Indeed, we can prove that for any $\bar{\rho} > 0.076$, the electric field is nowhere positive. We determine this critical value by first observing that the electric field achieves its maximum value at $\bar{x} = 0$. Setting $\bar{x} = 0$ in Eq. (6.69) gives this maximum value of $\overline{E}_z$ as

$$\ln\frac{1}{\bar{\rho}(2-\bar{\rho})} - 2 + \frac{2}{2-\bar{\rho}} - \frac{2(1-\bar{\rho})}{(2-\bar{\rho})}. \tag{6.70}$$

Setting Eq. (6.70) equal to zero and numerically solving gives $\bar{\rho} = 0.076$. Even when $\bar{\rho} < 0.076$, only the electric field in the central region becomes positive; the electric field close to the wires remains negative.

Eq. (6.69) was derived by making assumptions concerning the values of $\dot{I}$, $\dot{a}$, and $\dot{\rho}$ and should not be expected to hold rigorously. However, the conclusion that the effects of an expanding wire radius and decreasing wire separation cause a negative electric field for a large set of parameters is probably robust and can be expected to hold in general. Indeed, on the Solar Loop Experiment, the initial loop separation is about 8 cm and the initial loop radius is about 1.5 cm, giving $\bar{\rho} = 0.375$. On the Spheromak Experiment, the spider legs are flared and have different radii and separation distances at the cathode than at the anode. At the cathode, the spiders legs have have a radius of 0.2 cm and a separation of 4 cm, giving $\bar{\rho} \approx 0.1$. At the anode, the spider leg radius is 0.6 cm, and their separation is about 14 cm, so $\bar{\rho} \approx .09$. From these values, it seems likely that the dimensions of the Caltech plasma loops are such that the induced electric field, if axial, will be anti-parallel to the current and draw orbits inwards towards the magnetic null.

6.3.3 Drift Velocity

The purpose of this study was to determine how two adjacent plasma loops can merge into a single structure. It might seem somewhat circuitous, then, to assume that the plasma loops are expanding and to then show that the $\mathbf{E} \times \mathbf{B}$ drift is inward. We therefore compare the $\mathbf{E} \times \mathbf{B}$ drift with the velocity of the loops' boundaries. For larger values of $\bar{\rho}$, the $\mathbf{E} \times \mathbf{B}$ drift is larger than the boundary velocity, and we conclude that the merging process is accelerated the closer the loops get to each other because the $\mathbf{E} \times \mathbf{B}$ becomes larger.

The $\mathbf{E} \times \mathbf{B}$ drift is given by combining Eqs. (6.69) and (6.45),

$$\mathbf{v}_{\mathrm{ExB}} = \frac{\mathbf{E} \times \mathbf{B}}{B^2} = \frac{a/2}{\tau} \frac{1 - \overline{x}^2}{2\overline{x}} \left[\ln \frac{1 - \bar{x}^2}{\bar{\rho}(2 - \bar{\rho})} - \left(\frac{2}{1 - \bar{x}^2} - \frac{2}{2 - \bar{\rho}} \right) - \frac{2(1 - \bar{\rho})}{(2 - \bar{\rho})} \right] \hat{x}. \tag{6.71}$$

We will compare Eq. (6.71) with the velocity of the plasma boundaries given by $-\dot{a}/2 + \dot{\rho} = (a/2\tau)(1 + \overline{\rho})$. To start, we note that the two velocities are equal at the plasma surface. This is hardly coincidental; the electric field at the boundary is $\mathbf{E} = \mathbf{v} \times \mathbf{B}$, so the $\mathbf{E} \times \mathbf{B}$ drift at the boundary is

$$\frac{\mathbf{E} \times \mathbf{B}}{B^2} = -\frac{(\mathbf{v} \times \mathbf{B}) \times \mathbf{B}}{B^2} = \mathbf{v}. \tag{6.72}$$

However, away from the boundary, the $\mathbf{E} \times \mathbf{B}$ velocity may be greater or less than $\mathbf{v}$ depending on the value of $\bar{\rho}$. We plot Eq. (6.71) for several values of $\bar{\rho}$ in Fig. 6.10. When $\overline{\rho} = 0.5$, the $\mathbf{E} \times \mathbf{B}$ drift velocity is indeed greater than the speed of the plasma wall. However, at $\overline{\rho} = 0.15$, the two velocities have nearly the same value except at the vicinity of the null. For even lower values of $\overline{\rho}$, there are regions where the $\mathbf{E} \times \mathbf{B}$ drift is slower than the expansion rate of the tube. Of course, when $\bar{\rho} < 0.076$, the electric field becomes positive in the region around the null, and particle orbits are drawn away from the null rather than towards it.

This analysis suggests that the merging of two tubes may be a self-enhancing process. As the loops approach each other, the value of $\overline{\rho}$ increases, giving a faster and faster $\mathbf{E} \times \mathbf{B}$ drift towards the null. The particles on the outside of the flux tube are thus drawn to the null at a faster and faster rate.

6.4 Conclusions and Directions for Future Work

To explain the coalescence of the spider legs in the Caltech Spheromak Experiment into a single axisymmetric structure, we have studied the particle trajectories in a simplified model that treats the arched helical plasma loops as straight current-carrying wires. For a single wire, the particle trajectories all have the same qualitative behavior, but the addition of a second wire opens up new classes of trajectories: those that are confined to one wire, and those that are shared between both

wires. The time dependence of the Solar Loop and Spheromak experiments can cause transitions of confined orbits to shared orbits if the induced electric field is anti-parallel to the wire current. Unfortunately, we cannot presently determine the exact nature of the induced electric field from first principles, but we have argued that the induced electric field must be anti-parallel in the vicinity of the plasma loops when the loops move towards one another.

To further this work, the nature of the induced electric field in the actual experiments should be studied experimentally, as it seems unlikely that it can be determined by first principles alone due to the likely presence of plasma sheaths. If an experiment can determine the direction of the field, then the analysis of this chapter can proceed with confidence. The second set of information needed in the model is the experimental determination of the rate at which the plasma loops expand and attract. Once these parameters are determined, the analysis can proceed to determine exactly how fast orbits from the edge of the plasma loops are sucked into the magnetic null.

Finally, the current model does not investigate non-planar orbits. Analysis of such orbits is clearly more difficult than the study of planar orbits given the extra dimension of motion, and such studies of such orbits would probably proceed numerically. Note, though, that if an axial magnetic field were added to the model, then the field lines would be helical, and the planar orbits of the model presented in this chapter would not exist at all. Therefore, studies of non-planar orbits will be essential to more sophisticated models.

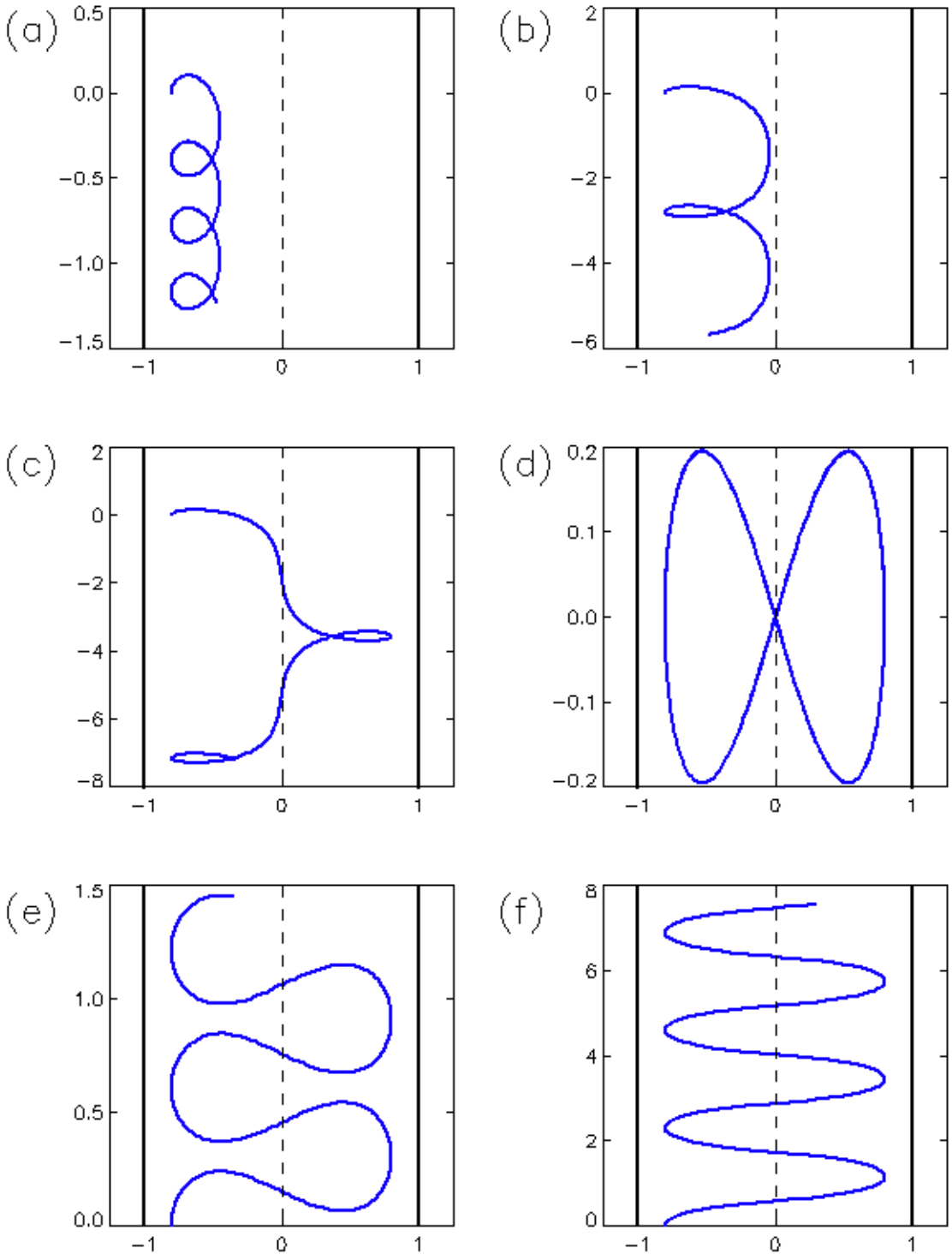

Figure 6.5: Several sample trajectories in the plane of two parallel wires. All orbits begin at $x = -0.8$ but with different velocities. (a) $v = 0.4$, well below the threshold to cross the magnetic null. The orbit is confined to the left wire. (b) $v = 0.51$, just below the threshold to cross the magnetic null. (c) $v = 0.511$, just above the threshold to cross the null. The orbit is symmetric between the two wires. (d) $v = 0.687994$, for which the orbit is closed. (e) $v = 0.8$, for which the z drift becomes positive. (f) $v = 1.4$, for which the particle never travels in the negative z direction.

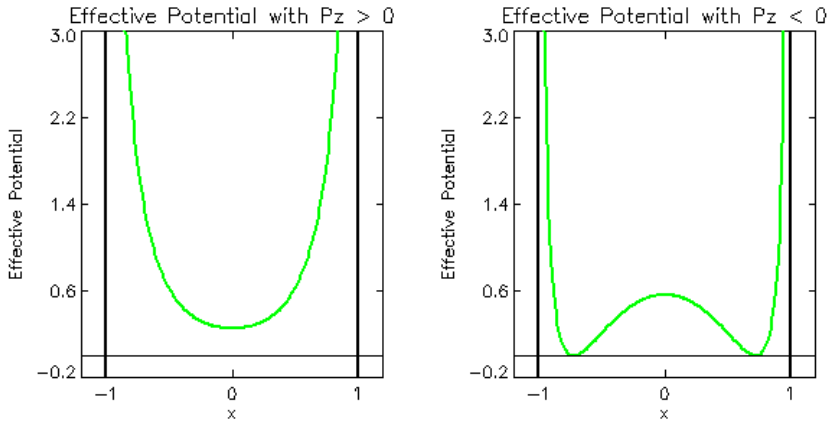

Figure 6.6: The effective potential for (a) $P_z < 0$ (b) $P_z > 0$. In (a), the potential forms a well with infinite walls, and the magnetic null $x = 0$ is a minimum. $P_z = 0.5$ for this particular plot. In (b), the potential well develops a central bump, and the magnetic null is a local maximum. Orbits with small energy can be trapped in one of the small wells, while orbits with sufficient energy can pass over the maxima at the null. This particular plot has $P_z = -0.75$.

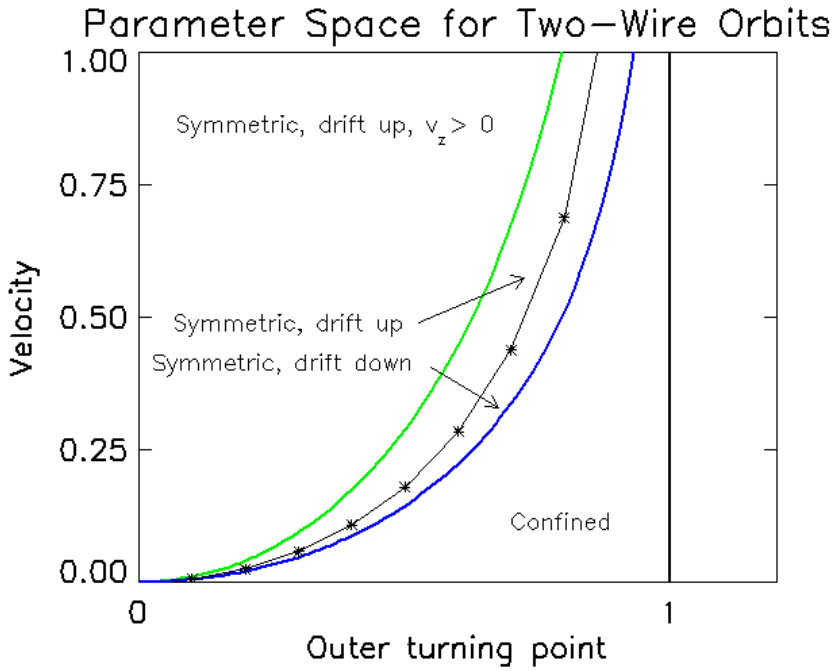

Figure 6.7: A parameter space plot of the different types of orbits. The bounding curves are determined by the values of the total velocity v and the canonical z momentum P_z. The points for which the orbits are closed are determined numerically at isolated points.

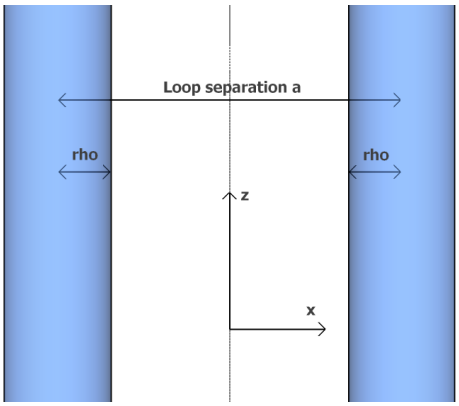

Figure 6.8: We align the z axis parallel to the current and denote the separation distance between the loops as a. We also give the loops a non-zero radius ρ, so the locations of the loops' edges, in the $y = 0$ plane, are $x = \pm(-a/2 + \rho)$.

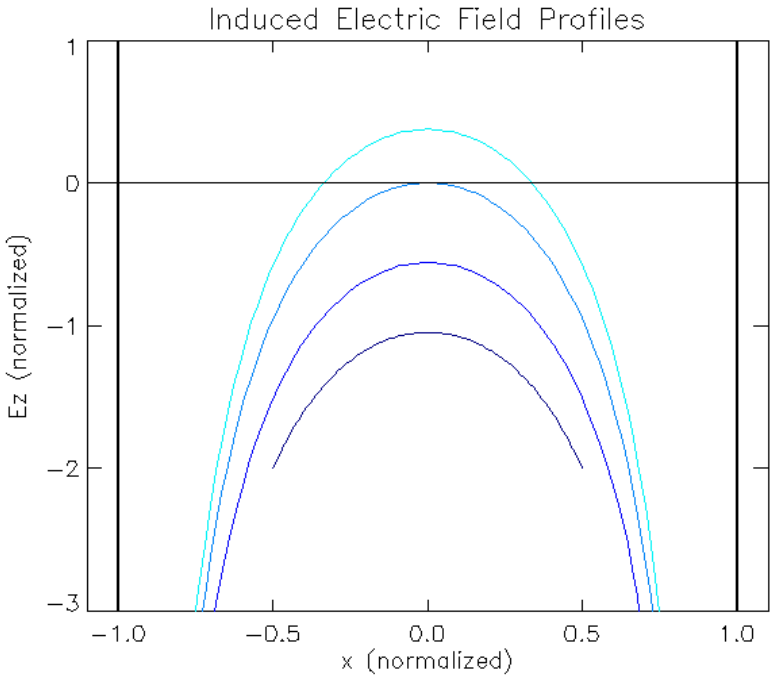

Figure 6.9: The electric field profile for different values of $\bar{\rho}$. Starting from the bottom curve, the $\bar{\rho}$ values are 0.5, 0.15, 0.076, and 0.05. $\bar{\rho} = 0.076$ is the critical value at which the electric field becomes positive for part of the domain.

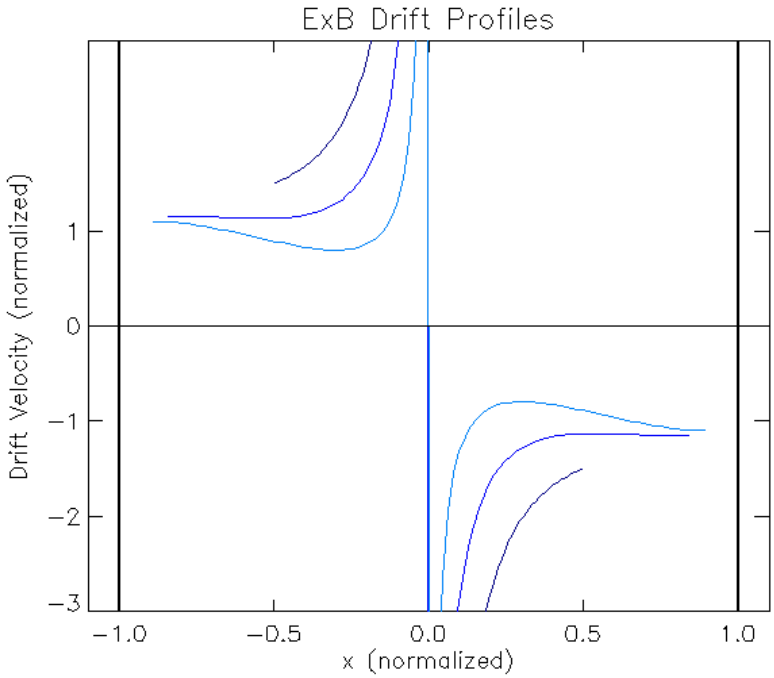

Figure 6.10: The $\mathbf{E} \times \mathbf{B}$ drift is plotted for a three different values of $\bar{\rho}$. The horizontal dashed lines denote the value of the plasma surface velocity. The top dark plot is for $\overline{\rho} = 0.5$; the $\mathbf{E} \times \mathbf{B}$ drift is quite large. The middle blue plot is for $\overline{\rho} = .015$; the drift velocity is nearly equal to the surface velocity over much of the domain. The bottom light-blue plot is for $\overline{\rho} = 0.1$; the $\mathbf{E} \times \mathbf{B}$ drift is slower than the surface velocity except near the null and the plasma surface.